SPECTROSCOPIC MONITORING OF ACTIVE GALACTIC NUCLEI FROM CTIO. I. NGC 3227

Cláudia Winge,[1,2,3] Bradley M. Peterson,[2] Keith Horne,[4,5] Richard W. Pogge,[2]
Miriani G. Pastoriza,[1,3] and Thaísa Storchi-Bergmann[1]

ABSTRACT

The results of a five-month monitoring campaign on the Seyfert 1.5 galaxy NGC 3227 are presented. Variability was detected in the continuum and in the broad emission lines. Cross correlations of the 4200 Å continuum light curve with the Hβ and He II λ4686 emission-line light curves indicate delays of 18 ± 5 and 16 ± 2 days, respectively, between the continuum variations and the response of the lines. We apply a maximum entropy method to solve for the transfer function that relates the Hβ and He II λ4686 lines and 4200 Å continuum variability and the result of this analysis suggests that there is a deficit of emission-line response due to gas along the line of sight to the continuum source for both lines. Using a composite off-nuclear spectrum, we synthesize the bulge stellar population, which is found to be mainly old (77% with age > 10 Gyr) with a metallicity twice the solar value. The synthesis also yields an internal color excess $E(B-V) \approx 0.04$. The mean contribution of the stellar population to the inner $5'' \times 10''$ spectra during the campaign was $\sim 40\%$.

Subject headings: galaxies: individual (NGC 3227) — galaxies: Seyfert — galaxies: stellar content

1. INTRODUCTION

Continuum and emission-line variability in active galactic nuclei (AGNs) has been detected over the last three decades (see Peterson 1988 for a review) and provides a valuable tool for understanding the radiative and dynamical processes inside these spatially unresolved sources. Within the last few years, intensive monitoring campaigns have provided enough data that more meaningful time-series analysis can be carried out in practice (e.g., Maoz et al. 1990, 1991; Clavel et al. 1991; Peterson et al. 1991, 1992, 1993, 1994; Stirpe et al. 1994a, b; Reichert et al. 1994; Wanders et al. 1993).

In this work, we present the results from an intensive ground-based spectroscopic monitoring campaign carried out at the Cerro Tololo Inter-American Observatory on the Seyfert 1.5 galaxy NGC 3227. This AGN has been studied over a wide range of wavelengths from X-rays (Tennant & Mushotzky 1983, Reichert et al. 1985) to radio (Ulvestad, Wilson, & Sramek 1981). Spectroscopic and photometric variability has been previously reported (Peterson, Crenshaw, & Meyers 1985; Quisbert et al. 1989). Recently, Salamanca et al. (1994, hereafter S94) presented the results of a LAG (Lovers of Active Galaxies) 1990 campaign on this same object.

2. DATA

The data consist of 26 spectra, obtained with the CTIO 1.0 m telescope and Cassegrain Spectrograph +2D-FRUTTI detector during the period 1992 January 1–June 9. This program was carried out in parallel with the NGC 3783 AGN

Watch campaign observations (Stirpe et al. 1994a). The instrumental setup was the same for all the observations, with a 5″ slit oriented E-W and spectral coverage from 3500 to 7200 Å. The resolution is 8 Å, measured from the full width at half-maximum (FWHM) of the comparison lines. The two-dimensional spectrograms were reduced according to IRAF standard procedures, and one-dimensional spectra were extracted in a 10″ window centered on the maximum of the continuum emission. The large slit width and extraction window ensure that basically all the slightly extended narrow-line region (NLR) emission (Durret 1989) is included in the final spectra, thus mitigating seeing effects. The spectra were flux calibrated using the standard spectrophotometric stars from Stone & Baldwin (1983), which were observed with a 10″ slit. Figure 1 shows the spectra of the minimum and maximum states observed during this campaign and Table 1 lists information relevant to the observations.

As a final step, the spectra were internally calibrated relative to each other with a variant of the method described by van Groningen & Wanders (1992). The program finds the optimum flux scaling factor, wavelength shift, and convolution factor for each spectrum with respect to a reference spectrum by varying these parameters until the residuals of one or more narrow lines (which are constant over the time scales of interest) in the difference between the two spectra are minimized. The JD 2,448,776 spectrum was used as reference and the residuals of the [O III] λ5007 line minimized. All spectra were scaled in flux so that $F([O III] \lambda5007) = 6.34 \times 10^{-13}$ ergs cm^{-2} s^{-1}. The resultant scaling factors are between 0.9 and 1.4, and the accuracy of the internal calibration, as judged from the [O III] residuals, is within 5%. A higher S/N ratio spectrum was obtained averaging all the individual spectra, except the JD 2,448,668, 2,448,724, 2,448,728, 2,448,760 (of lower S/N ratio due to the poor weather conditions), and will be referred to hereafter as the mean spectrum. All data were corrected for Galactic reddening [$E(B-V) = 0.005$; Burstein & Heiles 1984] and redshift, as measured using the strongest narrow emission lines on each spectrum. Flux scales and integrated flux measurements, however, have not been transformed to the rest frame of NGC 3227.

[1] Departamento de Astronomia, Universidade Federal do Rio Grande do Sul, Av. Bento Gonçalves, 9500, CP 15051, CEP91501-970, Porto Alegre, RS, Brasil; winge@if.ufrgs.br.

[2] Department of Astronomy, The Ohio State University, 174 West 18th Avenue, Columbus, OH 43210.

[3] Visiting Astronomer at the Cerro Tololo Inter-American Observatory of The National Optical Observatories, operated by AURA under contract with the National Science Foundation.

[4] Sterrekundig Instituut, University of Utrecht, P.O. Box 80000, NL-3508 TA, Utrecht, The Netherlands.

[5] Space Telescope Science Institute, 3700 San Martin Drive, Baltimore, MD 21218.
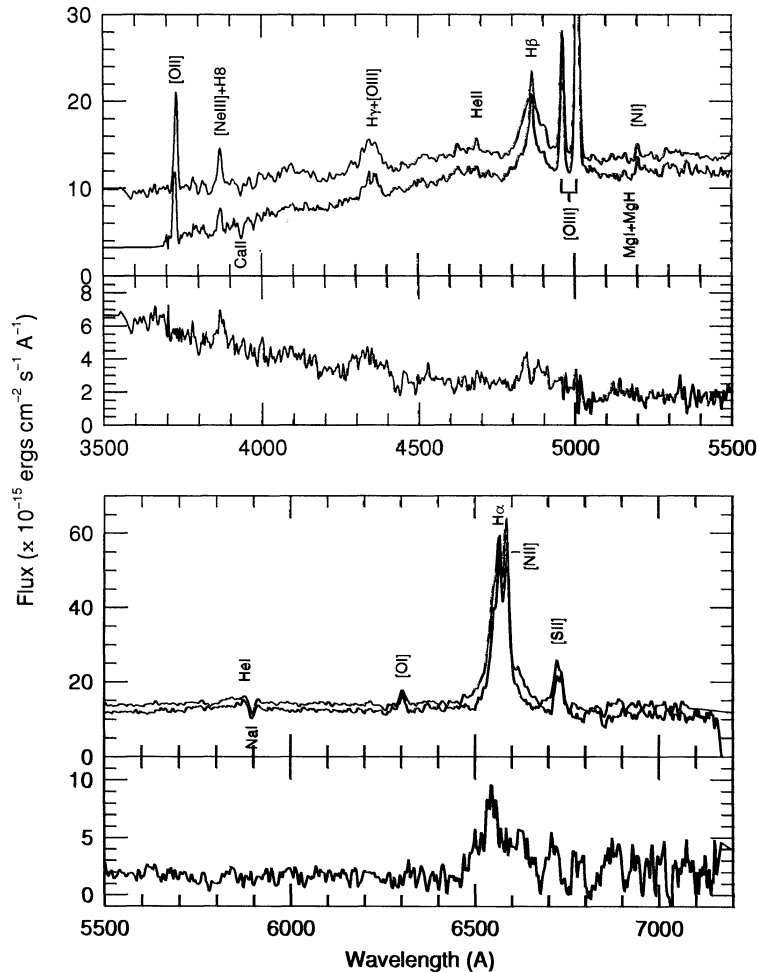
FIG. 1.—*Top panel*: representative spectra of the high (JD 2,448,631) and low (JD 2,448,704) states of activity in NGC 3227 observed during this campaign. The bottom panel shows the difference spectrum.

3. THE STELLAR POPULATION ANALYSIS

The spectra in Figure 1 show clear contamination from the underlying stellar population, as evidenced by the presence of the Ca II H and K, and the Mg I + MgH absorption lines. In order to assess the characteristics of this stellar population, we have extracted from the two-dimensional-spectrograms an off-nuclear spectrum corresponding to $5'' \times 10''$ regions centered at $20''.4$ E and W of the nucleus, corresponding to the bulge stellar population between 1150 and 1900 pc from the nuclear source (for $z = 0.0039$ and $H_0 = 75$ km s^{-1} Mpc^{-1}). These spectra were reduced and calibrated in the same manner as the nuclear spectra, co-added and normalized to an arbitrary flux scale. Table 2 gives the observed equivalent widths of the Ca II K $\lambda3933$, CN $\lambda4200$, CH G-band $\lambda4301$, and Mg I + MgH $\lambda5175$ absorption lines, and the intensity of the 4020 and 4570 Å continua relative to the 5870 Å continuum. These values were used to synthesize a stellar population template based on a library of star clusters (Bica 1988). The new version of the synthesis program (Schmitt et al. 1994) also gives an estimate of the intrinsic reddening.

The best solution is shown in Figure 2 together with the observed off-nuclear spectrum, and the synthetic equivalent widths and continua are listed in column (3) of Table 2. This template has a metallicity $[Z/Z_\odot] = 0.3$, and a 77% contribution at 5870 Å from a population older than 10 Gyr.

There is also a $\sim 10\%$ contribution at this same wavelength due to a very young (age $\leq 10^7$ yr) population. The internal reddening estimate obtained for the bulge of NGC 3227 is $E(B-V) \sim 0.04$.

We then attempted to estimate the stellar population contribution to the nuclear spectra. As all the spectra include the same extent of the underlying host galaxy, the stellar population contribution *in flux* is the same in all of them. Since the inclusion of a constant component in the measurements dilutes the amplitude of the actual continuum changes, it is important to determine the stellar contribution.

The method we used is the same described in S94. The measured equivalent width W_{AGN} of a given absorption feature, assumed to originate from the stellar population, but to some extent diluted by the AGN continuum, is compared with the equivalent width W_T of a spectrum of a normal galaxy template. This gives the fractional contribution of the stellar component to the observed continuum, which is then converted to a flux scale and appropriately subtracted. We consider here two cases: the stellar population contribution when the AGN continuum was in its minimum state during our campaign (JD 2,448,704), and that to the mean spectrum (the average over the whole period of observations). The former is the maximum percentile contribution of the stellar component, but the uncertainties will be greater due to relatively low S/N ratio of our

WINGE ET AL.

TABLE 1

OBSERVATION LOG

Julian Date (2,440,000+) (1)	UT Date (1992) (2)	Airmass (3)	Comments (4)	Scaling Factors (5)
8623..................	Jan 1	1.66	...	0.99
8627..................	Jan 5	2.31	...	1.15
8631..................	Jan 9	1.95	Cirrus	0.99
8635..................	Jan 13	1.74	...	1.07
8639..................	Jan 17	1.64	...	0.99
8647..................	Jan 25	2.01	...	1.26
8651..................	Jan 29	2.00	...	1.06
8656..................	Feb 3	1.76	...	0.95
8660..................	Feb 7	1.66	Cirrus	1.09
8664..................	Feb 11	1.75	...	0.91
8668..................	Feb 15	1.58	Clouds	1.34
8676..................	Feb 23	1.90	...	1.04
8678..................	Feb 25	1.87	...	0.98
8704..................	Mar 22	2.18	...	1.06
8712..................	Mar 30	1.77	...	1.27
8716..................	Apr 3	1.89	...	0.94
8720..................	Apr 7	1.83	...	1.02
8724..................	Apr 11	1.74	Clouds	1.24
8728..................	Apr 15	1.75	Clouds	1.12
8732..................	Apr 19	1.66	Haze	0.99
8736..................	Apr 23	1.65	...	1.03
8744..................	May 1	1.58	...	0.98
8760..................	May 17	1.71	Clouds	0.92
8763..................	May 20	1.58	Cirrus	1.42
8764..................	May 21	1.61	...	1.07
8776..................	Jun 2	1.63	...	1.00

individual spectra. The synthetic stellar population obtained above was used as the reference template.

The equivalent widths of the Ca II K $\lambda 3933$ and Mg I + MgH $\lambda 5175$ were measured in the observed spectra, and the results are listed in columns (4) and (5) of Table 2. The Mg I + MgH $\lambda 5175$ equivalent width was corrected for [N I] $\lambda 5199$ contamination as in S94. From the comparison between W_{AGN} and W_T, we obtain a stellar population contribution of 39% in the low-state spectrum and 38% in the mean one. The differences between the results obtained from the Ca II K $\lambda 3933$ and Mg I + MgH $\lambda 5175$ lines can be ascribed to the uncertainty in the placement of the continuum in the nuclear spectrum for the former due to the presence of the emission lines like Hδ and [Ne III] $\lambda 3968$ on either side of the absorption line, and the contamination of the later by the [N I] $\lambda 5199$ and/or Fe II emission lines.

Figure 3 shows the mean spectrum before (Fig. 3a) and after

(Fig. 3b) the subtraction of the synthetic stellar population template (Fig. 3c) scale to 38% of the mean continuum at 5180 Å. The residual Ca II K $\lambda 3933$ line is due to the lower resolution of the subtracted template. Notice that, even after the subtraction, the AGN continuum still does not show the characteristic "power-law plus blue-bump" shape usually seen in AGN spectra. The total Hα/Hβ ratio, obtained integrating the line fluxes above a local continuum within an interval of ± 5000 km s^{-1} of the systemic velocity after removing the [N II] $\lambda\lambda 6548$, 6584 lines contamination in Hα by fitting a multiple Gaussian profile to the blend, is 4.3, corresponding to a color excess $E(B-V) \approx 0.28$. If reddening corrected by this amount, the mean spectrum would rise toward the blue, but still show a turn-down at wavelengths shorter than ~ 4500 Å. If such feature was also due to reddening, the intervening absorbing material would be located between the continuum source and the BLR. There is also the possibility that the "blue bump" in this galaxy is intrinsically weak (McDowell et al. 1989). In this sense, the 1980–1983 IUE-averaged spectrum, as shown in the IUE-ULDA Access Guide No. 4 (Courvoisier & Paltani 1992), also presents a positive slope and some weak lines, both in emission and absorption. Even considering that the data were obtained 10 years apart, the overall shape is consistent with our optical spectrum and a strong contamination by a red stellar population. Although it is impossible to judge the actual strength of the underlying "power-law" continuum in the UV without a proper subtraction of the host galaxy contribution, it is clearly much less conspicuous in this object than in other low-luminosity Seyfert 1 galaxies (see, for example, the UV-to-IR atlas of Seyfert 1 spectra of Storchi-Bergmann et al. (1995). A downward curvature of the UV-optical spectrum and the absence of a "blue bump" in another very low luminosity Seyfert 1 galaxy, NGC 4593, has been recently discussed by Santos-Lléo et al. (1994). Finally, we had also explored the possibility of this residual turn-down in the optical spectrum being an artifact due to differential refraction losses (Filippenko 1982), but the calculations for a mean airmass sec $z = 1.80$, seeing width $\sim 1\overset{..}{.}5$ and position angle P.A. = 90°, indicate that the light loss relative to 5000 Å is less than 6% at ~ 3700 Å, and therefore not enough to explain the observed spectral shape.

4. VARIABILITY

After the correction for the host galaxy internal reddening $E(B-V) \sim 0.04$, as derived from the synthesis of the bulge

TABLE 2

STELLAR POPULATION ANALYSIS

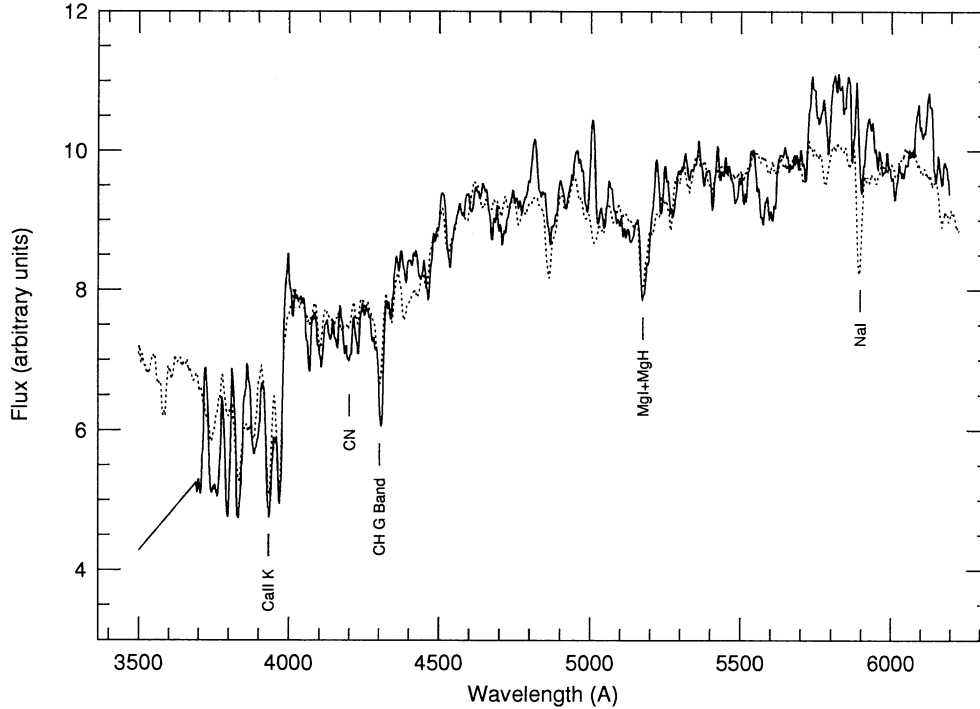| Feature (1)	Off Nucleus (2)	Template (3)	Mean (4)	Low State (5)
Equivalent Width (Å) and Continua Relative to 5870 Å = 10				
Ca II K $\lambda 3933$	10.0 ± 0.8	9.6 ± 0.5	3.4 ± 0.5	3.5 ± 0.6
CN $\lambda 4200$	8.9 ± 1.0	6.7 ± 0.8	...	...
CH G-band $\lambda 4301$	7.4 ± 0.8	6.3 ± 0.8	...	...
Mg I + MgH $\lambda 5175$......	6.2 ± 0.8	5.5 ± 0.6	1.2 ± 0.3	1.3 ± 0.4
4020 Å	0.73 ± 0.04	0.80 ± 0.09	...	...
4570 Å	0.87 ± 0.05	0.92 ± 0.01	...	...
Stellar Population Contribution (%)				
Ca II K $\lambda 3933$	...	...	41	43
Mg I + MgH $\lambda 5175$......	...	...	34	35
Average.................	...	...	38	39

FIG. 2.—The off nuclear spectrum (*solid line*) and the correspondent synthetic stellar population template (*dotted line*)

stellar population, a third-order polynomial continuum was fitted to each individual spectrum in 50 Å intervals centered at 3670, 4200, 5525, 6075, and 6990 Å and the He II $\lambda4686$, Hβ, He I $\lambda5876$, and Hα light curves were obtained by integrating all the flux above this continuum in the intervals 4575–4750 Å, 4750–4930 Å, 5550–6015 Å, and 6460–6680 Å, respectively.

The stellar population template, scaled to 38% of the mean flux at 5180 Å, was subtracted from the nuclear spectra and the 4200 and 5525 Å continua measured in two 50 Å bands. The flux measurements are listed in Table 3 and the light curves for the continua, He II $\lambda4686$ and Hβ are shown in Figure 4. The errors were obtained multiplying the rms of the continuum
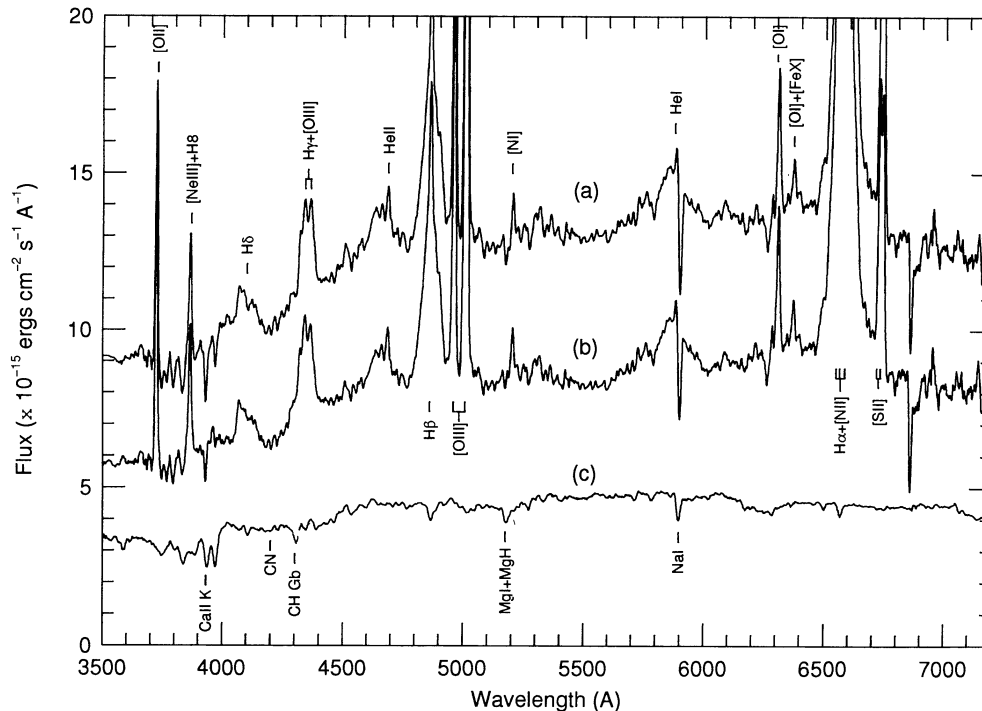
FIG. 3.—The nuclear mean spectrum before (*a*) and after (*b*) the subtraction of the stellar population template (*c*) as described in the text

TABLE 3
MEASUREMENTS OF SPECTRA[a]

Julian Date (2,440,000+) (1)	F_λ(4200 Å)[b] (2)	F_λ(5525 Å)[b] (3)	F(He II λ4686)[c] (4)	F(Hβ)[c] (5)	F(He I λ5876)[c] (6)	F(Hα)[c] (7)
8623	6.41 ± 0.18	8.53 ± 0.47	258.6 ± 16.9	583.5 ± 17.4	337.5 ± 54.8	3029.2 ± 51.9
8627	6.82 ± 0.23	9.02 ± 0.32	284.9 ± 23.8	648.4 ± 24.4	370.2 ± 63.7	3179.7 ± 34.9
8631	7.10 ± 0.25	8.71 ± 0.27	285.7 ± 21.9	646.1 ± 22.5	254.4 ± 45.5	2933.2 ± 29.6
8635	...	8.58 ± 0.21	244.7 ± 18.5	621.0 ± 19.0	269.5 ± 47.9	2926.0 ± 22.7
8639	8.08 ± 0.48	9.37 ± 0.44	268.3 ± 20.4	602.3 ± 28.7	302.3 ± 50.8	3093.8 ± 48.2
8647	8.03 ± 0.23	8.61 ± 0.31	281.6 ± 17.2	593.2 ± 17.6	409.5 ± 72.9	2837.9 ± 34.6
8651	7.48 ± 0.19	8.58 ± 0.33	299.4 ± 17.7	577.5 ± 18.2	310.7 ± 56.6	...
8656	...	8.28 ± 0.21	305.8 ± 21.5	607.5 ± 22.1	408.0 ± 48.6	3069.3 ± 23.0
8660	7.34 ± 0.32	8.88 ± 0.31	316.6 ± 24.5	601.3 ± 28.3	529.9 ± 72.8	3318.2 ± 34.5
8664	7.15 ± 0.21	8.37 ± 0.19	...	608.5 ± 18.1	...	...
8668	6.41 ± 0.41	...	372.8 ± 27.8	572.6 ± 30.9	...	3265.2 ± 64.3
8676	5.94 ± 0.35	7.85 ± 0.18	250.0 ± 20.5	603.7 ± 23.9	429.9 ± 41.9	...
8678	6.18 ± 0.22	8.58 ± 0.24	269.5 ± 20.1	570.0 ± 20.7	419.5 ± 56.2	3078.6 ± 26.7
8704	3.96 ± 0.25	6.86 ± 0.13	...	536.2 ± 17.1	379.8 ± 31.3	2440.2 ± 14.8
8712	5.55 ± 0.28	7.68 ± 0.33	206.8 ± 17.2	505.7 ± 23.1	353.4 ± 53.3	...
8716	5.74 ± 0.21	...	193.7 ± 20.7	465.9 ± 21.2	340.4 ± 61.5	2400.1 ± 29.2
8720	6.22 ± 0.28	8.32 ± 0.24	151.0 ± 15.7	467.8 ± 22.2	462.9 ± 55.5	2996.3 ± 26.3
8724	6.80 ± 0.51	...	...	...	...	...
8728	7.18 ± 0.56	10.11 ± 0.40	231.4 ± 33.6	455.7 ± 25.8	541.8 ± 91.8	3167.6 ± 43.5
8732	5.48 ± 0.66	7.51 ± 0.21	251.6 ± 20.3	520.3 ± 20.9	466.4 ± 49.6	2702.2 ± 23.5
8736	6.04 ± 0.25	7.87 ± 0.25	249.0 ± 21.9	607.5 ± 22.6	425.8 ± 58.4	2778.5 ± 27.7
8744	5.24 ± 0.39	7.08 ± 0.38	310.5 ± 25.0	549.6 ± 25.8	442.8 ± 67.5	2641.6 ± 41.5
8760	5.86 ± 0.37	7.38 ± 0.46	...	...	548.9 ± 77.9	3007.5 ± 73.9
8763	5.99 ± 0.38	7.49 ± 0.34	333.9 ± 23.4	561.0 ± 28.9	624.2 ± 79.5	3079.0 ± 37.7
8764	5.94 ± 0.36	...	320.6 ± 24.6	563.9 ± 26.4	...	2886.6 ± 35.1
8776	5.55 ± 0.29	7.45 ± 0.31	251.5 ± 21.4	528.6 ± 23.0	447.1 ± 71.1	2903.4 ± 33.7

[a] Corrected by $E(B-V) = 0.04$; see § 3.
[b] In units of 10^{-15} ergs cm^{-2} s^{-1} Å^{-1}.
[c] In units of 10^{-15} ergs cm^{-2} s^{-1}.

bands neighbor to each line by the width of the line integrating interval. The continuum errors are just the rms inside the respective bands. We excluded the epochs where the low S/N of the spectra (due to poor weather or full moon) or suspected calibration problems resulted in flux errors greater than 20%. Table 4 summarizes the general characteristics of the data base. The parameters F_{var} and R_{max} are the ratio of the rms fluctuation amplitude to the mean (corrected for the effect of measurement errors) and the ratio of maximum to minimum flux, respectively (see Clavel et al. 1991). Column (8) lists the reduced χ^2 for variability with respect to the mean. The constant flux hypothesis is strongly rejected in all cases $[P(\text{null}) < 10^{-4}]$.

4.1. Time-Series Analysis

In a standard reverberation scenario, the time delay between the continuum and BLR line emission variations is interpreted as an estimate of the BLR size. The delay can be obtained using both the interpolation cross-correlation (CCF) or discrete correlation (DCF) techniques. Although cross-correlation is a powerful method, this approach relies on several assumptions that are worth keeping in mind when interpreting the results (see Peterson 1993) for a review and discussion of the reverberation mapping process and its underlying assumptions and limitations. The details of the CCF and DCF calculations employed here are given by White & Peterson (1994). It has to

TABLE 4
VARIABILITY PARAMETERS AND SAMPLING CHARACTERISTICS

FEATURE (1)	NUMBER OF EPOCHS (2)	SAMPLING INTERVAL (days)		MEAN FLUX[a] (5)	F_{var} (6)	R_{max} (7)	χ^2_ν [b] (8)
		Average (3)	Median (4)				
F_λ(4200 Å)	24	6.65	4	6.35	0.14	2.04	12.13
F_λ(5525 Å)	22	7.29	4	8.23	0.09	1.47	9.54
He II λ4686	22	7.29	4	269.90	0.17	2.47	6.21
Hβ	24	6.35	4	566.57	0.10	1.42	5.73
He I λ5876	22	7.29	4	412.50	0.23	2.45	2.49
Hα	21	7.65	4	2940.7	0.08	1.38	9.97

[a] Units as in Table 3.
[b] Reduced χ^2 for variability about mean. Degrees of freedom are $N - 1$, where N is the number of epochs for each feature.
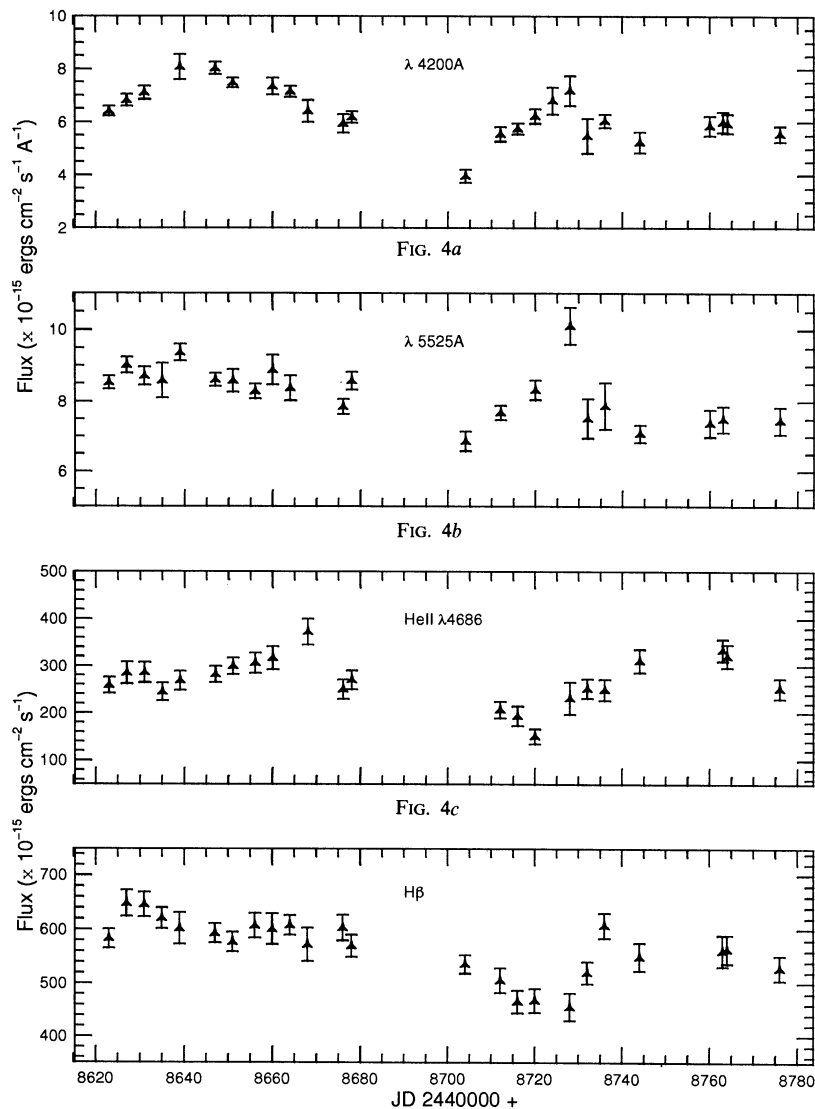
Fig. 4a

Fig. 4b

Fig. 4c

Fig. 4d

Fig. 4.—*From top to bottom:* (a) the 4200 Å continuum; (b) the 5525 Å continuum; (c) the He II λ4686; and (d) the Hβ light curves

be remembered also that the lags given by cross-correlation analysis can be misleading if interpreted directly as the physical dimensions of the BLR (Robinson & Pérez 1990; Pérez, Robinson, & de la Fuente 1992). In this regard, it is probably better to use the centroid, which is responsivity weighted, rather than the peak of the highest maximum of the CCF.

Because of the small amplitude of the Hα variations when compared with the internal scatter of the data, and to the large measurements errors in He I λ5876, the time series analysis for these two lines yields no conclusive results. The general behavior of the light curves is similar to the He II λ4686 and Hβ ones, and the width of the autocorrelation functions (see below) indicates that some real variations are indeed resolved.

The autocorrelation functions (ACFs) for the continua, He II λ4686, and Hβ (Gaskell & Peterson 1987) are shown in Figure 5, together with the sampling window autocorrelation functions for the 4200 Å continuum, and Hβ. The latter were produced averaging the ACFs of a light curve obtained by repeatedly sampling a white-noise spectrum in the same

pattern as the real observations. The FWHM of the sampling window indicates how much artificial correlation is introduced when the observed light curve is interpolated in order to calculate the CCF. The FWHM of the window ACFs are ~6 days for the 4200 Å continuum and line light curves. The line and continuum ACFs, on the other hand, are much broader than this (see Table 5), indicating that the variations on longer timescales are indeed resolved.

The results of the cross-correlation analysis are summarized in Table 5. Here Δt_{peak} is the lag at which the CCF reaches the maximum value, Δt_{cent} is the position of the CCF centroid, and r_{max} is the peak value. Figure 6 shows the 5525 Å continuum, Hβ, and He II λ4686 emission lines versus 4200 Å continuum CCFs as well as the DCFs calculated with a 6 day bin width. The 5525 Å versus 4200 Å CCF peaks at zero days, and the delays between the light curves of the emission lines and 4200 Å, as derived from the centroid of the CCF, is 18 and 16 days for Hβ and He II λ4686, respectively. These values can be interpreted as the luminosity-weighted radii of the BLR for the
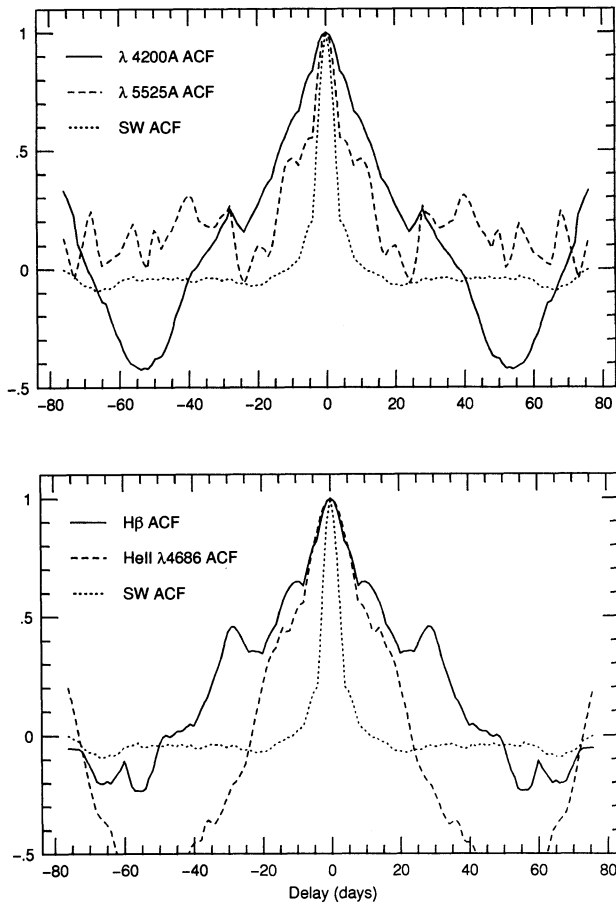
Fig. 5.—The autocorrelation functions: (*top*) 4200 Å (*solid line*), 5525 Å (*dotted line*), and 4200 Å sampling window (*dotted line*); (*bottom*) Hβ (*solid line*), He II λ4686 (*dotted line*), and Hβ sampling window.
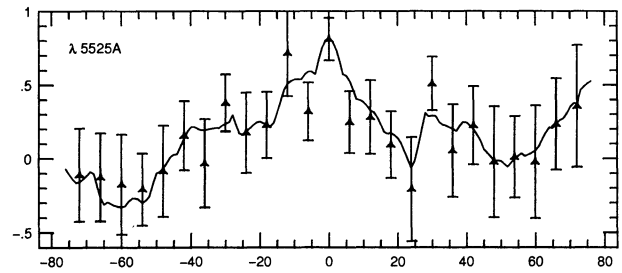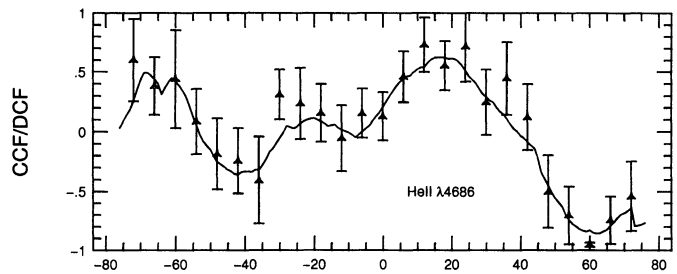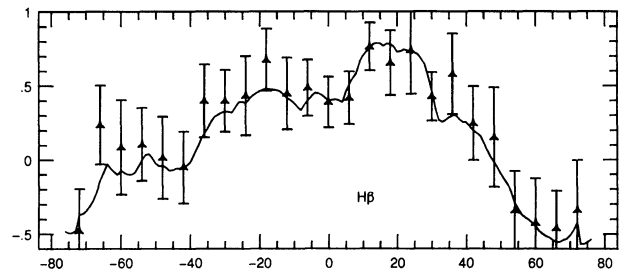

Fig. 6.—Cross-correlation and discrete correlation between the 4200 Å continuum and (*a*) the 5525 Å continuum; (*b*) the He II λ4686 emission line; and (*c*) the Hβ emission line light curves.

different lines (Robinson & Pérez 1990; Koratkar & Gaskell 1991). They are also in very good agreement with the result obtained by S94, where a time delay of 17 ± 7 days was found between the 6750 Å continuum and broad Hα light curves.

To assess the significance of our results and provide a meaningful estimate for the uncertainties in the measured delays, Monte Carlo simulations were employed, following the method described by Maoz & Netzer (1989). Starting with the observed continuum points, a model light curve is generated by interpolating linearly between observations separated by

more than one day and then smoothing the result. A model emission-line curve is then obtained by convolving the interpolated/smoothed continuum line curve with the transfer function for a thin spherical shell of radius R. The model light curves are then resampled at the same number of points as the observed ones so as to preserve the distribution of intervals between observations. Gaussian-distributed random noise comparable to the observational errors is added to each point, and the two data sets cross correlated to determine the location of the peak in the CCF. A minimum confidence level, based on the peak value of the CCF ρ is set as a condition for a given trial to be considered successful and the lag registered. The process is repeated a large number of times for a given R, varying the emission-line light curve sampling pattern, and the width of the resulting cross correlation peak distribution (CCPD) can be regarded as an estimate for the error in the observed delay.

The method used here, however, differs in a few details from the above. Since both continuum and light curves are measured from the same spectra, we modified the computing algorithm to include also a random resampling of the continuum light curve, preserving (1) the number of paired observations (i.e., the number of nights where it was possible to measure both continuum and line fluxes from the same spectrum); and

TABLE 5

VARIABILITY ANALYSIS

First Series (1)	Second Series (2)	FWHM (days) (3)	Δt_{peak} (days) (4)	Δt_{cent} (days) (5)	r_{max} (6)
4200 Å ACF	...	25.2	...	...	...
5525 Å ACF	...	13.5	...	...	...
He II λ4686 ACF......	...	21.4	...	...	...
Hβ ACF	...	28.6	...	...	...
He I λ5876 ACF	...	17.5	...	...	...
Hα ACF	...	15.4	...	...	...
4200 Å	5525 Å	21.7	0	0	0.815
4200 Å	He II λ4686	26.8	16	16	0.790
4200 Å	Hβ	26.5	14	18	0.625

(2) the distribution of intervals between emission-line observations only (i.e., the distribution of intervals between continuum points is randomly changed at each iteration). The motivation behind this alteration is twofold: to include the effect of possible correlated errors due to the simultaneous measurement of points in both light curves, and to assess the errors originated from the sparse sampling of the continuum light curve. Furthermore, the distribution is computed for the centroid of the CCF rather than the peak, as the former is the quantity we are considering as representative of the BLR size.

The geometry assumed is a thin spherical shell of radius $R = 18$ and 16 light days, for Hβ and He II $\lambda4686$, respectively, with no emission-line asymmetry. The distributions of 500 trials at a 99% confidence level ($\rho = 0.515$ and 0.537 for $N = 24$ and 22 points, respectively) are shown in Figure 7. The results indicate uncertainties of ±2 and ±5 days for the response of He II $\lambda4686$ and Hβ, respectively, to the 4200 Å continuum variations. We also considered the case of anisotropic line emission, which we model in terms of a parameter A such that the cloud emissivity as a function of angle from the line of sight θ (as seen from the central source) is $I(\theta) = 1 + A \cos\theta$; $A = 0$ corresponds to completely isotropic line emission, and $A = 1$ corresponds to completely aniso-

tropic emission, i.e., with all of the line response directed back towards the continuum source (see Ferland et al. 1992). For the case $A = 1$, we find that the BLR radius inferred from the time delay is smaller by a factor $1 + A/3$, as expected, but that the uncertainties are unchanged. Other simple geometries will yield similar results. In other words, the lag is observationally a well-determined quantity, but interpretation beyond inferring some scale length R/c is dependent on the BLR geometry and physical conditions in the clouds and thus remains problematic.

4.2. *Echo Mapping Analysis*

The relationship between the continuum light curve $C(t)$ and the emission-line light curve $L(t)$ can be written

$$L(t) = \int_{-\infty}^{\infty} \Psi(\tau)C(t - \tau)d\tau , \qquad (1)$$

where $\Psi(\tau)$ is the transfer function (TF) (Blandford & McKee 1982) that describes the responsivity distribution of the BLR gas as seen by an external observer. The aim of a reverberation study is to invert equation (1) to solve for $\Psi(\tau)$. With a limited amount of irregularly sampled data, this can be done by employing a maximum entropy method, as described by Horne, Welsh, & Peterson (1991) and by Peterson et al. (1993), in which case equation (1) takes the form

$$L(t) - \bar{L} = \int_{0}^{\tau_{max}} \Psi(\tau)[C(t - \tau) - \bar{C}]d\tau , \qquad (2)$$

where $\bar{L}$ and $\bar{C}$ are the line and continuum background levels, respectively, and τ_{max} the maximum delay considered for the calculations.

The MEMECHO code (Horne, Welsh, & Peterson 1991) uses a maximum entropy technique to fit the data by adjusting the continuum light curve, the line transfer function, and the line background level, while holding fixed the continuum background level. The solution we consider here set the continuum background level to the median of the continuum data points, but the results are not sensitive to this arbitrary choice.

Figure 8 shows three MEMECHO fits to the observed continuum, Hβ, and He II $\lambda4686$ light curves. The model continuum light curves found in these three fits are shown as continuous curves snaking through continuum measurements in the lower panel of the figure. The reconstructed transfer functions for Hβ and He II $\lambda4686$ are shown in the upper left panels. The corresponding model line light curves are compared with the line flux measurements in the upper right panels. Horizontal dashed lines indicate the continuum and line background levels. In each case the model line light curve is obtained by subtracting the continuum background level from the continuum light curve, convolving the difference light curve with the transfer function, and then adding the line background level.

A good fit to the data is ensured by imposing for each of the three light curves a constraint of the form $\chi^2/N = 1$, where N is the number of observations.[6] The solutions are qualitatively similar with $\chi^2/N = 0.7, 1, 1.4$. The constraints provided by the measured data points and their error bars leave considerable ambiguity in such a fit, but much of this is eliminated by our
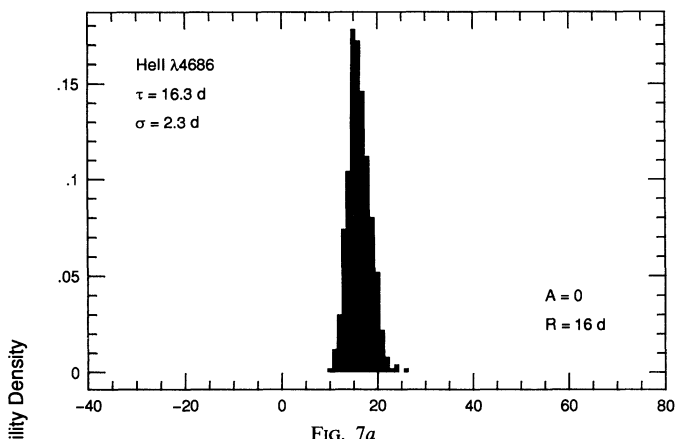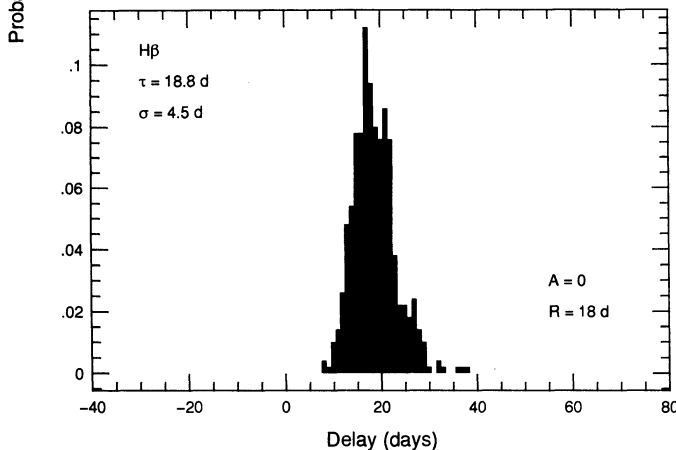
FIG. 7.—Probability distributions of the centroid of the cross-correlation curves for (*a*) He II $\lambda4686$, and (*b*) Hβ obtained through Monte Carlo simulations for the indicated geometries (*lower right; R* = shell radius, *A* = emission-line asymmetry). The most probable lags and associated uncertainties are shown at the upper left.

[6] Notice that the method employed here does not impose that the distribution of the residuals from the fit must be normal (by performing a Kolmogorov-Smirnov test) as a constraint on the solutions. As a result, some of the observed points deviate strongly from the recovered TF.
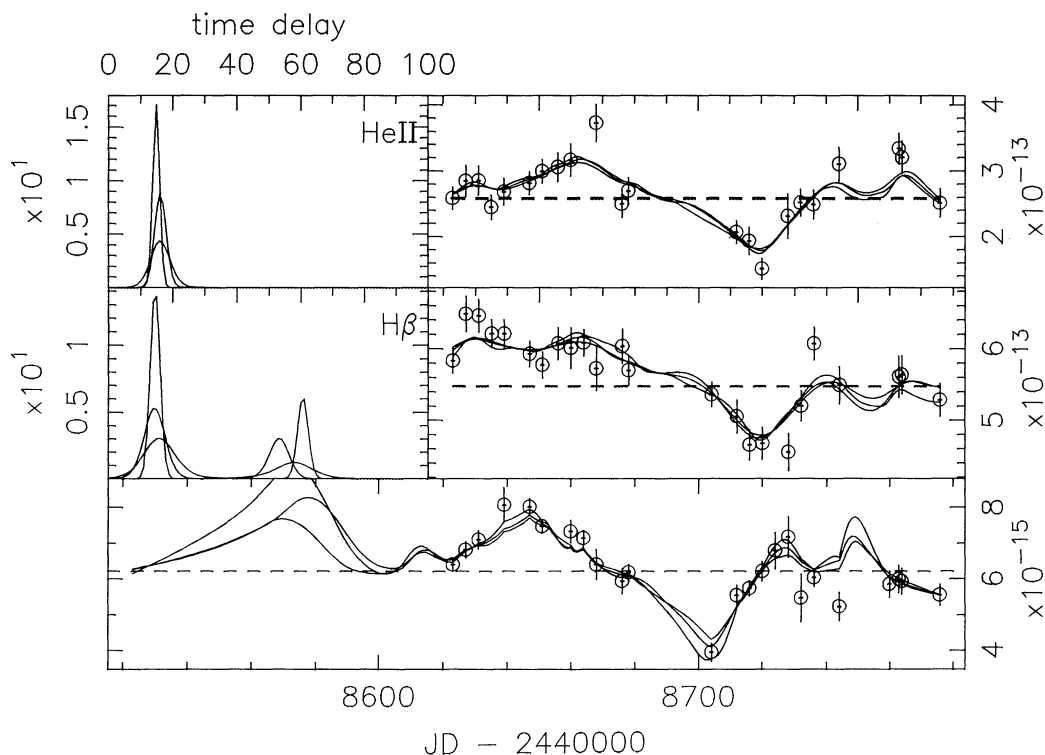
Fig. 8.—Solutions for the He II $\lambda4686$ and Hβ transfer functions for three different values of the "stiffness" parameter $W = 0.1, 1, 10$. The bottom panel shows the maximum entropy fits to the observed continuum light curve. The transfer functions are shown in the upper left panels, and in the upper right panels, the observed He II $\lambda4686$ and Hβ line fluxes are fitted by a convolution of the respective transfer function and the continuum light curve. The dashed horizontal lines are the mean values of the light curves.

requirement that the transfer functions and the continuum light curve be strictly positive and "as smooth as possible" in a precisely defined sense. Much of the remaining ambiguity in the solution is explored in Figure 8 by comparing the results found for three values of the control parameter $W = 0.1, 1, 10$, progressively increasing the "stiffness" of the transfer functions relative to the continuum light curve. There is evidently uncertainty in the widths and positions of the transfer function peaks, and in the shape of the continuum light curve prior to the first data point and in the larger gaps between data points. The solution with $W = 0.1$ has sharper transfer function peaks and smaller continuum fluxes near JD 2,448,590 and 2,448,750.

The He II $\lambda4686$ transfer function has a single peak near 15 days, indicating that the He II $\lambda4686$ flux measurements are consistent with a light curve that has the same shape as the continuum light curve but is delayed in time by ~ 15 days. This delay seems to be well established by the minimum observed at JD 2,448,720 in the He II $\lambda4686$ light curve corresponding to the minimum at JD 2,448,705 in the continuum. The width of the peak is not well defined. The peak can be arbitrarily sharp ($W \rightarrow 0$), but a full-width at half-maximum more than ~ 10 days is not possible without introducing an implausible level of excursions in the gaps between data points. In particular, the He II $\lambda4686$ response is clearly much lower at a lag of 0 than it is at the peak.

The Hβ transfer function in these solutions exhibits two peaks, one centered near 15 days, and a smaller one near 50–60 days. The main peak is determined in a manner similar to the He II $\lambda4686$ peak, by the minimum in the Hβ light curve near JD 2,448,720. The width of the Hβ peak is similarly indeter-mined, although it is somewhat wider than the He II $\lambda4686$

peak reflecting the wider dip in the light curve. The secondary Hβ peak near 50–60 days combines with the peak in the con-tinuum at JD 2,448,560–80 to boost the Hβ fluxes near the beginning of the experiment.

Figure 9 exhibits slightly different solutions that we obtained by fitting the Hβ and He II $\lambda4686$ light curves separately, using a different continuum light curve for each line. In this case both lines have transfer functions that peak near 18 days, and the Hβ transfer function no longer develops the second peak.

All our fits yield transfer functions with the prompt line response at a lag of zero much lower than the delayed peak response at lags of 14–18 days. These characteristics would seem to be robust features based on the measured light curves. Fits with $\chi^2/N = 1$ and monotonically decreasing transfer functions were found, but they are unacceptable because they have impossibly large excursions in most of the gaps between data points. If the standard assumptions of the echo mapping analysis are correct, namely, that the line variations arise as delayed versions of the continuum variations due to light travel time between a compact continuum source and a more extended emission-line region, then the conclusion is that there is a deficit of line response along the line of sight to the contin-uum source. This requires a nonspherical geometry (Horne, Welsh, & Peterson 1991), or an inwardly directed anisotropy of the line emission (Ferland et al. 1992). Similar results have been found for the Hβ line in NGC 5548 (Peterson et al. 1994) and Mrk 590 (Peterson et al. 1993).

The second peak in the Hβ light curve is based primarily on the observed Hβ fluxes being high near the beginning of the experiment. If real, this second peak would imply that the Hβ emission-line region consists of two distinctly separated and
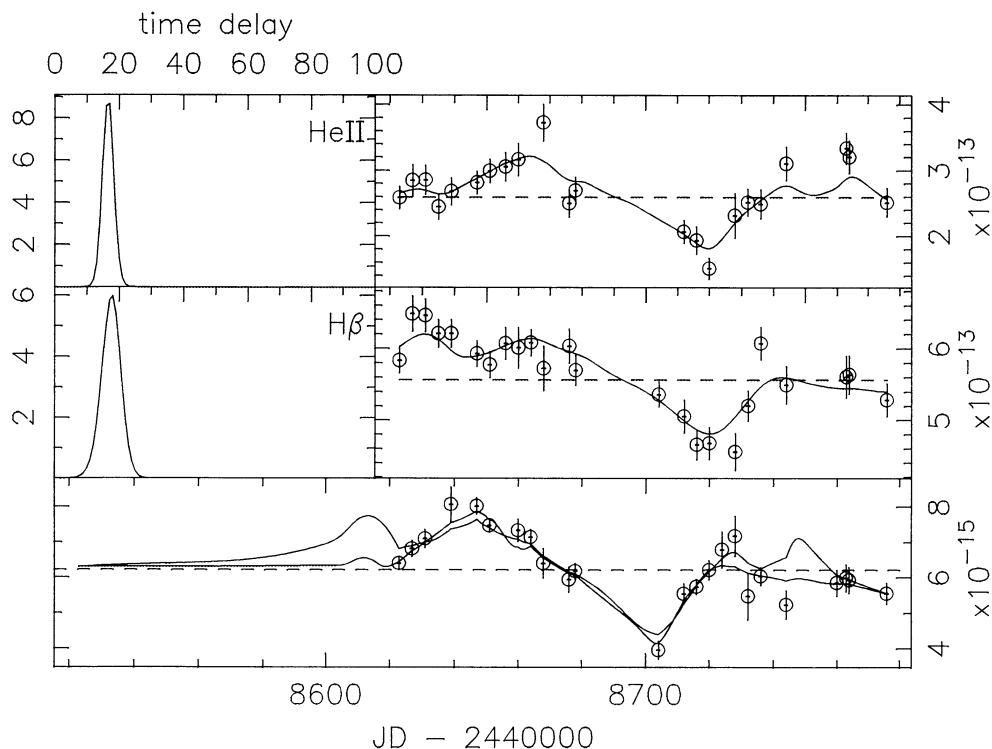
Fig. 9.—Solutions for the He II λ4686 and Hβ transfer functions with independent MEM fits to the observed continuum light curve ($W = 1$). Format as in Fig. 8. Both solutions peak at 18 days and the Hβ secondary peak is absent.

relatively small parts. This structure can be confirmed by continued monitoring observations.

5. CONCLUSIONS

We have monitored the variability of the optical continuum and broad emission lines in the spectrum of the Seyfert galaxy NGC 3227 between 1992 January and June, and the main results of this campaign can be summarized as follows.

Continuum and broad line variability is detected and resolved. The cross-correlation analysis between the 4200 Å continuum and the Hβ and He II λ4686 emission lines reveals that the variations in the lines follow those in the continuum by 18 ± 5 and 16 ± 2 days, respectively. The continua at 4200 and 5525 Å are found to vary in plase within the resolution of our experiment (~ 4 days). A maximum entropy method was employed to solve for the Hβ and He II λ4686 transfer functions in this source, and both lines show a deficit of response at small delays, with Hβ presenting a secondary peak at longer lags. The width of the transfer function peaks is not well defined, but the data allow us to rule out solutions with significant response at zero delay. The reality of the Hβ secondary peak can be confirmed with further monitoring of this source.

An analysis of the bulge stellar population indicates that the stellar content in our spectra is mainly old, with a 2 times solar metallicity, and that there is an internal color excess of $E(B-V) \sim 0.04$ in the inner regions of the bulge. The mean contribution of the stellar population to the nuclear spectra during this campaign was $\sim 40\%$. After the subtraction of this component, the nuclear spectrum does not show the presence of the "big blue bump" feature. This might be either an intrinsic characteristic of the object or attributable to reddening interior to the BLR. Although there is some indication of the presence of absorption material inside the emission-line regions, the latter possibility seems unlikely since the evidence for dust in AGN suggests that it is outside rather than interior to the BLR.

REFERENCES

Bica, E. 1988, A&A, 195, 76
Blandford, R. D., & McKee, C. 1982, ApJ, 255, 419
Burstein, D., & Heiles, C. 1984, ApJS, 54, 33
Clavel, J., et al. 1991, ApJ, 366, 64
Courvoisier, T. J.-L., & Paltani, S. 1992, IUE-ULDA Access Guide, No. 4 (Noordwijk: ESA Pub. Div.)
Durret, F. 1989, A&AS, 81, 253

Ferland, G. J., Peterson, B. M., Horne, K., Welsh, W. F., & Nahar, S. N. 1992, ApJ, 387, 95
Filippenko, A. V. 1992, PASP, 94, 715
Gaskell, C. M., & Peterson, B. M. 1987, ApJS, 65, 1
Horne, K., Welsh, W. F., & Peterson, B. M. 1991, ApJ, 367, L5
Koratkar, A. P., & Gaskell, C. M. 1991, ApJS, 75, 719
Maoz, D., & Netzer, H. 1989, MNRAS, 236, 21

Maoz, D., et al. 1990, ApJ, 351, 75
———. 1991, ApJ, 367, 493
McDowell, J. C., Elvis, M., Wilkes, B. J., Willner, S. P., Oey, M. S., Polomsky, E., Bechtold, J., & Green, R. F. 1989, ApJ, 245, L13
Pérez, E., Robinson, A., & de la Fuente, L. 1992, MNRAS, 255, 502
Peterson, B. M. 1988, PASP, 100, 18
———. 1993, PASP, 105, 247
Peterson, B. M., Crenshaw, D. M., & Meyers, K. A. 1985, ApJ, 298, 283
Peterson, B. M., et al. 1991, ApJ, 368, 119
———. 1992, ApJ, 392, 470
———. 1994, ApJ, 425, 622
Peterson, B. M., Ali, B., Horne, K., Bertram, R., Lame, N. J., Pogge, R. W., & Wagner, R. M. 1993, ApJ, 402, 469
Quisbert, J., Binette, L., Daltabuit, E., & Cantó, J. 1989, PASP, 101, 1078
Reichert, G. A., Mushotzky, R. F., Peter, R., & Holt, S. S. 1985, ApJ, 296, 69

Reichert, G. A., et al. 1994, ApJ, 425, 582
Robinson, A., & Pérez, E. 1990, MNRAS, 244, 138
Salamanca, I., et al. 1994, A&A, 282, 742 (S94)
Santos-Lléo, M., Clavel, J., Barr, P., Glass, I. S., Pelat, D., Peterson, B. M., & Reichert, G. 1994, MNRAS, in press
Schmitt, H. R., & Bica, E. L. D. 1995, in preparation
Stirpe, G. M., et al. 1994a, ApJ, 425, 609
———. 1994b, A&A, 285, 857
Stone, R. P. S., & Baldwin, J. A. 1983, MNRAS, 204, 347
Storchi-Bergmann, T., Kinney, A., & Challis, P. 1995, ApJS, 98, 103
Tennant, A. F., & Mushotsky, R. F. 1983, ApJ, 264, 92
Ulvestad, J. S., Wilson, A. S., & Sramek, R. A. 1981, ApJ, 247, 419
van Groningen, E., & Wanders, I. 1992, PASP, 104, 700
Wanders, I., et al. 1993, A&A, 269, 39
White, R. J., & Peterson, B. M. 1994, PASP, 106, 879